DOI: 10.1002/ejic.201100084

Theoretical Study of Phosphorescence of Iridium Complexes with Fluorine-Substituted Phenylpyridine Ligands

Xin Li,[a,b] Boris Minaev,[b,c] Hans Ågren,*[b] and He Tian*[a]

Keywords: Iridium / Fluorine / Organic light-emitting diodes / Phosphorescence / Density functional calculations

Time-dependent density functional theory (TD-DFT) with linear and quadratic response approaches was applied to calculate absorption and luminescence spectra of a number of facial and meridional iridium complexes with fluorine-substituted phenylpyridine ($F_n$ppy) ligands. The absorption and luminescence spectra were studied to simulate the photophysical properties of electroluminescent devices fabricated on the basis of these iridium complexes used to increase spin–orbit coupling and the triplet-state blue emission of the corresponding organic light-emitting diodes (OLEDs). By using the quadratic response technique, the phosphorescence radiative rate constant and lifetime of the studied iridium complexes were calculated through spin–orbit coupling perturbation and compared with the measured data in experiments. A satisfactory agreement between these data permits us to guide improvements in the design of phosphorescence-based OLEDs by predicting the structure–property relationships through quantum chemical calculations.

Introduction

Heavy-transition-metal complexes, particularly iridium(III) and platinum(II) compounds, that contain large π-conjugated ligands, such as phenylpyridines (ppy), bipyridines (bpy), and porphyrins, have received tremendous interest because of their potential for full utilization of both the singlet and triplet excitons upon electron–hole annihilation in organic light-emitting diodes (OLEDs).[1–5] At the same time, an enhanced triplet generation following photoinduced charge transfer (CT) has recently been reported in organic donor–acceptor polymer blend films that are important for use in photovoltaic devices.[6,7] In all these applications, the singlet–triplet (S–T) transitions are strongly enhanced relative to typical organic polymer films, like polyphenylene vinylene (PPV), usually applied in molecular electronics.[2]

Such electroluminescent devices typically consist of few layers of a luminescent organic polymer film, like PPV, sandwiched between two metal electrodes. Upon an applied bias, the electrons and holes are injected from the metal electrodes into the polymer. When these opposite-charged carriers start to migrate through the organic polymer, they can form nearest-neighbor excitons. In this case, the nongeminate pair of the oppositely charged polarons (produced independently at different electrodes) recombines and captures each other, being excited by charge transfer between the singly occupied molecular orbital (SOMO) of the electron carrier and the lowest unoccupied molecular orbital (LUMO) of the hole. Since the charge pairs are nongeminate, they have random spin orientation; thus the singlet and triplet colliding pairs are equally probable.[8] In general, the triplet state has three spin projections ($M_S = 0, \pm 1$) and the singlet spin state has only one microstate ($M_S = 0$). The singlet excitons in PPV and in other organic conjugated polymers provide intense luminescence. On the other hand, the radiation from the triplet excitons is spin-forbidden and is therefore much less intense in organic species.[9–11] This triplet–singlet ($T_1 \rightarrow S_0$) transition from the lowest triplet excited state to the singlet ground state provides the phosphorescence, which is about seven to eight orders of magnitude weaker than the fluorescence (the $S_1 \rightarrow S_0$ transition) of organic polymers.[10,11] On this background it has been commonly assumed that the quantum yield of electroluminescence in such OLEDs has an upper statistical limit of 25%.[12] The triplet excitons in pure organic polymers are dark and spend 75% of the electric energy of the recombination of charge carriers just to heat the polymer.

The spin-forbidden phosphorescent $T_1 \rightarrow S_0$ transition can acquire dipole activity through spin–orbit coupling (SOC); this perturbation is very weak in organic π-conjugated polymers because the orbital angular momentum matrix elements between the optically active singlet and triplet π–π* states of the conjugated systems are negligible,[9,10] and orbital magnetization is practically quenched in such

[a] Key Laboratory for Advanced Materials and Institute of Fine Chemicals, East China University of Science and Technology, Shanghai 200237, People's Republic of China
E-mail: tianhe@ecust.edu.cn
[b] Department of Theoretical Chemistry, School of Biotechnology, Royal Institute of Technology, 106 91 Stockholm, Sweden
E-mail: agren@theochem.kth.se
[c] Bogdan Khmelnitskij National University, 18031 Cherkassy, Ukraine

organic dyes.[11] The second reason for weak phosphorescence relates to the absence of heavy elements in a pure organic system; the SOC-induced splitting in the carbon atom is a thousand times smaller than the splitting of multiplets in the iridium or platinum ions.[11,13] Thus the strength of the SOC-induced mixing between the singlet and triplet manifolds and release of spin-selection rules is much more efficient in species that contain heavy elements.[14]

To enhance the OLED electroluminescence and to enforce the triplet excitons to work as light emitters, Baldo and Forrest et al.[1–3,15,16] decided to incorporate a special dye into an organic polymer that contained a heavy element, which could provide strong SOC to overcome spin-prohibition for the $T_1 \rightarrow S_0$ transition. The first prototype of such a dye was tris(2-phenylpyridine)iridium, or the [Ir(ppy)$_3$] complex,[2] the strong phosphorescence of which has been widely studied by theoretical[14,17,18] and experimental photophysical methods.[1,19–24] The incorporation of [Ir(ppy)$_3$] into a polymer thus leads to efficient OLED devices, and a large variety of similar composite materials have therefore been synthesized.[2–5,12,25–28] They now constitute an important class of organic polymers, which are doped by a heavy-atom-containing dye to increase the electroluminescence of the OLEDs.[20,23,29]

In particular, recently synthesized organometallic complexes of the iridium ion with various organic π-conjugated ligands have become quite popular in the OLED fabrication community because of the strong phosphorescence in the visible region.[19,23,28,30–36] The anionic 2-phenylpyridine (ppy), acetylacetonate (acac), 2-carboxy-4-aminopyridine, and neutral bipyridine (bpy) ligands, in different combinations with the iridium(III) ion, provide effective phosphorescent complexes.[22,23,30–33,37,38] They also have an advantage that their emission color can be tuned from blue to red by the peripheral functionalization of the ligands with electron-donating and electron-withdrawing substituents.[23,30,37,38]

A fundamental understanding from the first principles of the energy, charge, and spin transport, including their intrinsic transformations in organic polymers doped with iridium complexes, is highly important for development of new effective OLEDs. In this paper we present density functional theory (DFT) studies on the phosphorescence of organometallic iridium(III) complexes with fluorine-substituted 2-phenylpyridine (F$_n$ppy) ligands. The aim of the paper is to calculate the optical properties of some new facial (*fac*-) and meridional (*mer*-) [Ir(F$_n$ppy)$_3$] complexes because of their significance for OLED applications.[23] First-principles theoretical analysis of the phosphorescence of such organometallic compounds is available with the Dalton program package.[39]

We present connections between features of electronic structures and photophysical properties including the phosphorescence efficiency and energy-transfer mechanisms of the $T_1 \rightarrow S_0$ transition of such systems. Electric dipole transition moments were calculated by time-dependent density functional theory (TD-DFT) using quadratic response (QR) functions[40] to interpret the high efficiency of the OLED devices that contain these organometallic compounds.

Results and Discussion

Structures of S_0 and T_1 States

The chemical structures of the iridium complexes are shown in Figure 1. In the present work we are interested in the structures of the singlet ground state (S_0) and the first triplet excited state (T_1) since both are involved in the phosphorescence process. The relevant bond lengths are gathered in Table 1, in which the bond lengths of the *fac*-[Ir(ppy)$_3$] and *fac*-[Ir(tpy)$_3$] [tpy denotes the 2-(*p*-tolyl)pyridine ligand] complex obtained through X-ray or electron diffraction measurements[41–43] are included for comparison. For completeness, the structure of the prototype *fac*-[Ir(ppy)$_3$] complex, which has been extensively studied in experiments, is also computed and presented together with the [Ir(F$_n$ppy)$_3$] complexes. The calculated structure of the *fac*-[Ir(ppy)$_3$] complex shows partial agreement with experimental structures. Compared with *fac*-[Ir(tpy)$_3$], the Ir–N bond length in *fac*-[Ir(ppy)$_3$] is 0.02 Å longer, and the Ir–C bond length is 0.015 Å shorter, which can be attributed to the steric hindrance effect of the methyl group in the tpy ligand. The Ir–N and Ir–C bond lengths in *fac*-[Ir(F$_n$ppy)$_3$] complexes are very close to those in *fac*-[Ir(tpy)$_3$], thereby suggesting a similar steric effect of the fluorine atoms. Besides, it is interesting to find in *mer*-[Ir(F$_n$ppy)$_3$] that the Ir–C^2 bond is significantly shorter than the other two Ir–C bonds and that the Ir–N^3 bond is the longest Ir–N bond. Moreover, in *mer*-[Ir(F$_n$ppy)$_3$] the Ir–C^2 bond is perpendicular to the other two Ir–C bonds, and the Ir–N^3 bond is also perpendicular to the other two Ir–N bonds. Overall, the hybrid PBE0 functional along with the mixed basis set of the LANL2DZ and 6-31G* type predict satisfactory bond lengths for the iridium complexes compared with those obtained through X-ray or electron diffraction, in accord with the results reported by Nie et al.[44] and of our previous work.[45] All of the [Ir(ppy)$_3$] and [Ir(F$_n$ppy)$_3$] complexes have been calculated without symmetry restraints, although the optimized *fac* complexes turned out to be close to the C_3 symmetry.

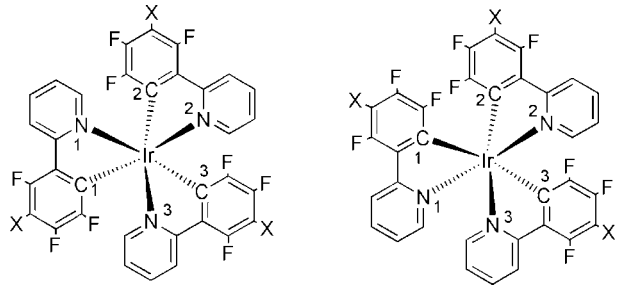

Figure 1. Chemical structures of the iridium complexes: *fac*-[Ir(F$_n$ppy)$_3$] (left) and *mer*-[Ir(F$_n$ppy)$_3$] (right). X represents H (n = 3) or F (n = 4) atom.

Table 1. Optimized S_0 and T_1 bond lengths [Å] for [Ir(ppy)$_3$] and [Ir(F$_n$ppy)$_3$].

	State	Ir–N^1	Ir–N^2	Ir–N^3	Ir–C^1	Ir–C^2	Ir–C^3
fac-[Ir(ppy)$_3$]	S_0	2.152	2.151	2.151	2.008	2.009	2.009
	T_1	2.164	2.174	2.122	2.020	2.007	1.967
fac-[Ir(F$_3$ppy)$_3$]	S_0	2.134	2.134	2.135	2.019	2.019	2.018
	T_1	2.146	2.143	2.097	2.027	2.015	1.996
fac-[Ir(F$_4$ppy)$_3$]	S_0	2.134	2.133	2.131	2.021	2.021	2.020
	T_1	2.147	2.151	2.110	2.031	2.016	1.977
mer-[Ir(F$_3$ppy)$_3$]	S_0	2.063	2.048	2.160	2.069	2.007	2.086
	T_1	2.064	2.048	2.122	2.072	2.014	2.073
mer-[Ir(F$_4$ppy)$_3$]	S_0	2.064	2.048	2.156	2.070	2.009	2.087
	T_1	2.075	2.046	2.130	2.081	2.017	2.045
exp. *fac*-[Ir(ppy)$_3$][41]	S_0	2.088			2.006		
exp. *fac*-[Ir(ppy)$_3$][42]	S_0	2.158			2.033		
exp. *fac*-[Ir(tpy)$_3$][43]	S_0	2.132			2.024		

Unfortunately, we have not found any reported bond length numbers for the T_1 structure. In comparing the predicted changes in bond length of the optimized S_0 and T_1 structures, we notice that in the *fac*- and *mer*-[Ir(F$_n$ppy)$_3$] complexes one of the ppy ligands comes closer to the central iridium atom and the other two ligands get pushed away. In the *fac*-[Ir(ppy)$_3$] and *fac*-[Ir(F$_n$ppy)$_3$] complexes, the Ir–N^1 and Ir–C^1 bonds are both elongated around 0.01 Å. The Ir–N^2 bond is elongated by 0.01–0.02 Å, whereas the Ir–C^2 bond is hardly affected. The Ir–N^3 and Ir–C^3 bonds are significantly shortened by 0.02–0.04 Å. The structural change in *mer*-[Ir(F$_n$ppy)$_3$] has a clear direction; the Ir–C^2 bond is elongated, whereas the Ir–N^3 bond is shortened. These two bonds are the special bonds that are perpendicular to their counterparts. The Ir–C^3 bond is also shortened together with the Ir–N^3 bond. Along with the changes in the Ir–N and Ir–C bond lengths, some internal deformations also occur in the ligands. All of the molecules undergo rather significant structural changes during the $S_0 \rightarrow T_1$ transition. The changes in bond length can be understood by looking at the molecular-orbital (MO) plots in Figure 2, which indicate that the $S_0 \rightarrow T_1$ transition constitutes a charge transfer from the 5d metal orbital to the ligands. After relaxation at the triplet state, the electron distribution localizes to the ligands, which then moves closer to the iridium atom. Such a transition was assigned as a metal-to-ligand charge transfer (MLCT) in character by Hay,[17] who has considered the vertical $S_0 \rightarrow T_1$ excitation in similar systems. Further insight could be gained by analyzing the frontier molecular orbitals of these iridium complexes.

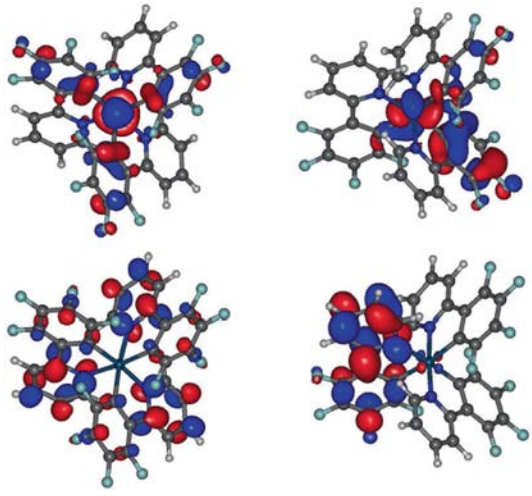

Figure 2. Calculated HOMOs (top) and LUMOs (bottom) of the iridium complexes: *fac*-[Ir(F$_4$ppy)$_3$] (left) and *mer*-[Ir(F$_4$ppy)$_3$] (right).

Frontier Molecular Orbitals and Excitation Energies

The calculated highest occupied molecular orbital (HOMO) and lowest unoccupied molecular orbital (LUMO) in *fac*-[Ir(F$_4$ppy)$_3$] and *mer*-[Ir(F$_4$ppy)$_3$] are shown in Figure 2, visualized by using the Gabedit software.[46] The HOMO and LUMO in *fac*-[Ir(F$_3$ppy)$_3$] and *mer*-[Ir(F$_3$ppy)$_3$] are similar in shape and therefore not shown. In both *fac*-[Ir(F$_n$ppy)$_3$] and *mer*-[Ir(F$_n$ppy)$_3$], the HOMO–LUMO transitions show a mixed character of the MLCT and the intraligand π–π* transitions. In general, the HOMO has only partial d(Ir) character, with the remainder of the orbital being localized at the π MOs of the ligands, mostly at the phenyl parts of the ppy ligands, the pyridine parts being practically empty. Specifically, in *mer*-[Ir(F$_n$ppy)$_3$] only the phenyl unit that contains the C^2 atom contributes significantly to the HOMO, the Ir–C^2 bond being perpendicular to the other two Ir–C bonds. In *fac*-[Ir(F$_n$ppy)$_3$], all ppy ligands contribute to the LUMO, whereas in *mer*-[Ir(F$_n$ppy)$_3$] only the ppy ligand that contains the N^3 atom contributes, with its Ir–N^3 bond perpendicular to the other two Ir–N bonds. The special shapes of the HOMO and LUMO in the *mer*-[Ir(F$_n$ppy)$_3$] complexes might be the origin of the low quantum yield in solution;[23] previous studies have shown that the quantum efficiency of the phosphorescence emission is significantly depressed when the LUMO is dominantly contributed by an ancillary ligand as in [(ppy)$_2$Ir(bza)],[16] [(ppy)$_2$Ir(dbm)],[47] [(pmb)$_2$Ir(acac)],[48] and [(ppy)$_2$Ir(pic)].[49]

The HOMO–LUMO energy-level diagram for these compounds is shown in Figure 3. In the *fac* isomers it can be seen that the introduction of the fluorine atoms lowers the energy levels of HOMO/LUMO and enlarges the HOMO–LUMO energy gap, thereby leading to blueshifted emission.

The green-emitting *fac*-[Ir(ppy)$_3$] becomes the blue-emitting *fac*-[Ir(F$_n$ppy)$_3$] complexes after fluorination on the ppy ligands. In the *mer*-[Ir(F$_n$ppy)$_3$] complexes, the HOMO–LUMO energy gaps are 0.3 eV smaller than their *fac* isomers. Further inspection of the coefficients of molecular orbitals reveals that the iridium contribution to the HOMO follows the order *fac*-[Ir(F$_3$ppy)$_3$] > *fac*-[Ir(F$_4$ppy)$_3$] > *mer*-[Ir(F$_3$ppy)$_3$] > *mer*-[Ir(F$_4$ppy)$_3$], thus showing the effect of the fourth electron-withdrawing fluorine atom and of the facial-to-meridional isomerization.

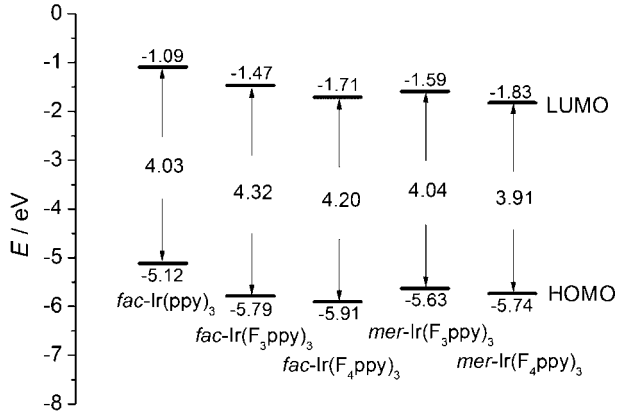

Figure 3. Calculated energy-level diagram of HOMOs and LUMOs in the iridium complexes *fac*-[Ir(ppy)$_3$], *fac*-[Ir(F$_n$ppy)$_3$], and *mer*-[Ir(F$_n$ppy)$_3$].

For the [Ir(F$_n$ppy)$_3$] complexes, the excitation energies were calculated by TD-DFT methods with the PBE0 functional and the mixed basis set of LANL2DZ and 6-31G*. The conductor-like polarizable continuum model (C-PCM)[50,51] was used to simulate the solvent effect of dichloromethane used in the experiments.[23] The absorption spectrum was then simulated by using the Lorentzian convolution with a half-bandwidth of 0.2 eV, as shown in Figure 4. All spectra show strong π–π* peaks around 240 and 290 nm, and the MLCT transitions at longer wavelength are relatively weak compared to the intraligand π–π* transitions, in accord with the measured absorption spectra.[23] At the absorption peaks around 290 nm, the fourth fluorine atom introduced into the phenyl ring of the ppy ligand gives rise to a slight increase in the absorption intensity as well as a small blueshift in the absorption wavelength. The introduction of the fourth fluorine atom also results in a redshift in the weak MLCT absorption bands. Compared to experimental absorption spectra, which show that the two maximal peaks lie at around 235 and 285 nm in the *fac* isomers and 255 and 300 nm in the *mer* isomers,[23] the TD-DFT calculations nicely reproduce the absorption bands of the iridium complexes, although the wavelengths are slightly underestimated for the *mer*-[Ir(F$_n$ppy)$_3$] complexes. Furthermore, TD-DFT can provide insights into the singlet MLCT excitations. In the *fac*-[Ir(F$_3$ppy)$_3$] and *fac*-[Ir(F$_4$ppy)$_3$] complexes, the MLCT bands are identified at 355 and 363 nm, respectively, which correspond to electron transitions from HOMO to LUMO, LUMO+1, and LUMO+2, the latter MOs being localized on two or three ppy ligands. For the *mer* isomers the MLCT bands lie at about 10 nm lower energy than their facial counterparts, and the LUMO, LUMO+1, and LUMO+2 are localized on the single ppy ligand.

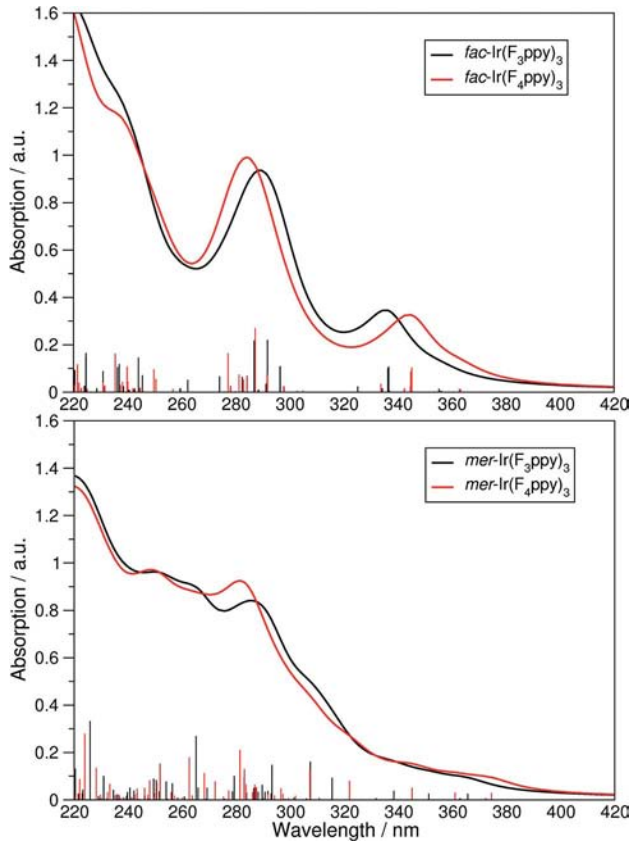

Figure 4. Calculated absorption spectra for the iridium(III) complexes.

Phosphorescence Wavelength and Lifetime

In the present work we have calculated by the TD-DFT QR technique the $S_0 \rightarrow T_1$ transition moment with the ground-state equilibrium structure. In Table 2 we present the calculated 0–0 transition energies and the singlet–triplet transition energies together with the experimental values.[20,23,52] The 0–0 transition energy is calculated as the energy difference between the optimized S_0 state and T_1 state, according to the so-called ΔSCF method. The S–T transition energy is computed by the linear-response TD-DFT approach implemented in the Dalton code. From Table 2 it can be seen that the 0–0 transition energy of *fac*-[Ir(ppy)$_3$] is overestimated by around 0.15 eV, which might be attributed to structural distortion in the solid state.[42] The 0–0 transition energies for the *fac*- and *mer*-[Ir(F$_n$ppy)$_3$] complexes are reproduced with better accuracy, within 0.1 eV. It is interesting to observe that the computed S–T transition energy is very close to the calculated 0–0 transition energy, although they have different physical meanings.

Table 2. Calculated phosphorescence emission wavelengths along with experimental data.

	$\Delta E_{0-0,exp.}$ [eV, nm]	$\Delta E_{0-0,calcd.}$ [eV, nm]	$\Delta E_{S-T,calcd.}$ [eV, nm]
fac-[Ir(ppy)$_3$]	2.47, 503[a] 2.46, 505[b]	2.61, 475	2.61, 475
fac-[Ir(F$_3$ppy)$_3$]	2.77, 448[c]	2.82, 440	2.84, 437
fac-[Ir(F$_4$ppy)$_3$]	2.73, 455[c]	2.71, 458	2.74, 452
mer-[Ir(F$_3$ppy)$_3$]	2.77, 448[c]	2.85, 435	2.84, 436
mer-[Ir(F$_4$ppy)$_3$]	2.72, 456[c]	2.79, 445	2.75, 450

[a] In CH_2Cl_2 at 4.2 K.[52] [b] In THF at 30 K.[20] [c] In butyronitrile glass at 77 K.[23]

Listed in Table 3 are the theoretically calculated radiative rate constants, $k_{r,calcd.}$. The k_r of *fac*-[Ir(ppy)$_3$] is to be compared with the high-temperature limit of k in tetrahydrofuran (THF) and the thermal average of k_r in poly(methylmethacrylate) (PMMA). It should be noted that the high-temperature limit of k in THF is obtained by fitting to the experimental data in low-temperature THF glass (1.2–130 K), in which the nonradiative processes are suppressed. Therefore, the similarity between the high-temperature limit of k in THF and the calculated k_r of *fac*-[Ir(ppy)$_3$] confirms the accuracy of the computations. The calculated k_r of *fac*-[Ir(ppy)$_3$] is slightly smaller than the thermal average of k_r in PMMA; still they are of the same order of magnitude. The computed k_r of *fac*- and *mer*-[Ir(F$_n$ppy)$_3$] complexes are to be compared with experimental radiative rate constants obtained from the lifetime and quantum yield: $k_{r,exp.} = \Phi_{em}/\tau_0$. The k_r values are overestimated in *fac*-[Ir(F$_3$ppy)$_3$], underestimated in *mer*-[Ir(F$_3$ppy)$_3$], and better reproduced for the [Ir(F$_4$ppy)$_3$] complexes. The accuracy of the theoretical computation is satisfactory considering the fact that $k_{r,calcd.}$ and $k_{r,exp.}$ are of the same order of magnitude. Moreover, the computed k_r values show consistent features: (1) the introduction of fluorine atoms in the ppy ligand leads to a decrease in k_r, and (2) the *mer* isomers have smaller k_r than the *fac* isomers.

Normally the fluorine atom is thought to enlarge the SOC effect and therefore the radiative rate constant through the so-called heavy-atom effect.[53,54] However, fluorine is also known to diminish the $S_0 \rightarrow T_1$ transition dipole moment by destroying the balance of different S–S and T–T contributions.[55] In magnesium tetraphenylporphines, it has been proposed that the presence of a few fluorine substitutions on the phenyl rings could enhance the mixing between the triplet states, thereby resulting in blueshifted phosphorescence wavelength and longer lifetime.[56] The bromine atom in bromomethylcarbene has also been suggested to show an inverse heavy-atom effect that decreases the SOC strength.[57] In this study, the introduction of fluorine atoms in the ppy ligands shows similar effects that give rise to smaller radiative rate constant k_r (Table 3) and longer lifetime τ (Table 4), in agreement with experimental observations. Therefore DFT calculations are able to reveal the heavy-atom effect or the inverse heavy-atom effect, which is not intuitively predictable, thus showing the usefulness in facilitating better design of OLED materials.

Table 4. Calculated phosphorescence lifetimes along with experimental values.

	$\tau_{exp.}$ [μs]	$\tau_{calcd.}$ [μs]	τ^x [μs]	τ^y [μs]	τ^z [μs]
fac-[Ir(ppy)$_3$]	1.4[a] 2.0[b]	2.1	1.4	1.4	246.9
fac-[Ir(F$_3$ppy)$_3$]	3.9[c]	2.7	1.7	1.9	220.2
fac-[Ir(F$_4$ppy)$_3$]	4.2[c]	3.2	2.2	2.0	290.4
mer-[Ir(F$_3$ppy)$_3$]	3.9[c]	4.7	3.3	3.1	140.9
mer-[Ir(F$_4$ppy)$_3$]	4.4[c]	6.4	4.4	4.3	167.0

[a] In PMMA at ambient temperature.[52] [b] In THF at 130 K.[20] [c] In butyronitrile glass at 77 K.[23]

It is also interesting to consider the SOC matrix element $\langle S_0|\hat{H}_{SO}|T_1\rangle$, which reflects the nonradiative quenching of the triplet state T_1. From Figure 2 it can be seen that the iridium contribution to LUMO is smaller in *fac*-[Ir(F$_4$ppy)$_3$] than in *mer*-[Ir(F$_4$ppy)$_3$], thus leading to the qualitative conclusion that the SOC matrix element between the S_0 and T_1 states is smaller in the facial isomer. By performing quantitative calculations with the use of DFT and the linear response method, the SOC matrix element between the S_0 and T_1 states was determined to be around 100 cm^{-1} in the *fac*-[Ir(F$_n$ppy)$_3$] and 500 cm^{-1} in the *mer*-[Ir(F$_n$ppy)$_3$] complexes. Considering the fact that the square of the SOC matrix element $\langle S_0|\hat{H}_{SO}|T_1\rangle$ determines the nonradiative quenching rate of the T_1 state to the ground S_0 state, the emission quantum yields in the *mer* isomers were expected to be much smaller than those in the *fac* isomers, in agreement with experimental measurements.[23] Besides, it should be noted that $\langle S_0|\hat{H}_{SO}|T_1\rangle$ also contributes to the $S_0 \rightarrow T_1$ transition intensity through the difference between the permanent dipole moments of the T_1 and S_0 states, according to Equation (1). In the facial complex this dipole moment difference is negligible, and the main source of the $S_0 \rightarrow T_1$ transition intensity arises from the intensity borrowing from the $T_1 \rightarrow T_n$ and $S_0 \rightarrow S_n$ transitions. In meridional isomer, the difference between the permanent dipole moments of

Table 3. Calculated phosphorescence radiative rate constants along with experimental data.

	$k_{r,exp.}$ [s^{-1}]	$k_{r,calcd.}$ [s^{-1}]	k_r^x [s^{-1}]	k_r^y [s^{-1}]	k_r^z [s^{-1}]
fac-[Ir(ppy)$_3$]	4.8×10^5[a], 6.9×10^5[b]	4.8×10^5	7.3×10^5	7.1×10^5	4.0×10^3
fac-[Ir(F$_3$ppy)$_3$]	1.9×10^5[c]	3.8×10^5	5.9×10^5	5.3×10^5	4.5×10^3
fac-[Ir(F$_4$ppy)$_3$]	2.3×10^5[c]	3.2×10^5	4.5×10^5	4.9×10^5	3.4×10^3
mer-[Ir(F$_3$ppy)$_3$]	4.3×10^5[c]	2.1×10^5	3.0×10^5	3.3×10^5	7.1×10^3
mer-[Ir(F$_4$ppy)$_3$]	1.6×10^5[c]	1.6×10^5	2.3×10^5	2.3×10^5	6.0×10^3

[a] High-temperature limit of k in THF.[20] [b] Thermal average of k_r in PMMA.[52] [c] In degassed CH_2Cl_2 at 298 K.[23]

the T_1 and S_0 states and their mutual SOC matrix element are non-negligible and provide destructive contribution to the total $S_0 \rightarrow T_1$ transition moment.

The calculated $S_0 \rightarrow T_1^i$ radiative lifetimes τ^i for the three spin sublevels of the first triplet excited state are presented in Table 4. Each spin sublevel provides its own polarization for the $S_0 \rightarrow T_1$ transition. The calculated phosphorescence lifetime τ for *mer*-[Ir($F_n$ppy)$_3$] is nearly as twice large as those for the *fac*-[Ir($F_n$ppy)$_3$] complexes. From Equations (2) and (3) we see that the phosphorescence lifetime is inversely proportional to the cube of the emission energy and the square of the transition dipole moment. The calculated phosphorescence wavelengths are similar for the *mer* and *fac* isomers (Table 2), thereby indicating that notable difference arises in the calculated transition dipole moment.

As described above, the computed k_r values are self-consistent and provide insight into the effects of the fluorine atoms in ppy ligands, and so are the calculated radiative lifetimes, which are equal to the inverse of k_r. It should be noted that the nonradiative processes are not taken into account in theoretical computations, and therefore the calculated lifetime can only be compared with the experimental lifetime measured in a low-temperature glass or polymer matrix in which the nonradiative processes are suppressed. The calculated τ for *fac*-[Ir(ppy)$_3$] is larger than the lifetime in PMMA at ambient temperature and is very close to that observed in THF at 130 K. Since the $\tau_{exp.}$ in THF has reached its high-temperature limit at 130 K,[20] it must be considered that the theoretical computation has nicely reproduced the experimental results. The τ values are underestimated for *fac*-[Ir($F_n$ppy)$_3$] and overestimated for the *mer* isomers. Since the experimental measurements for *fac*-[Ir($F_n$ppy)$_3$] are carried out at 77 K, the zero-field splitting cannot be ruled out, and it is reasonable that the experimental lifetimes are slightly larger than the theoretical thermal limit. From this point of view, the calculated τ values in *fac*-[Ir($F_n$ppy)$_3$] are consistent with the experimental results. For the *mer*-[Ir($F_n$ppy)$_3$] complexes, the k_r values have been nicely reproduced in the calculations (Table 3), whereas the calculated lifetimes are larger than those measured in butyronitrile glass, which might be attributed to possible structural distortion in the solid state.

Conclusion

We have presented time-dependent density functional theory (TD-DFT) quadratic response calculations of the phosphorescence rate constants and lifetimes of organometallic complexes of an iridium ion with fluorine-substituted 2-phenypyridine (ppy) ligands. The ground-state bond lengths of the central iridium atom were compared with the prototype *fac*-[Ir(ppy)$_3$] and *fac*-[Ir(tpy)$_3$] complexes, for which tpy denotes the 2-(*p*-tolyl)pyridine ligand, and good agreement has been achieved at the advised density-functional level of theory. The HOMOs of these complexes are mainly localized on the metal center and the phenyl ring of the ppy ligands, whereas the LUMOs are delocalized on the ppy ligands. It was found that the iridium contribution to the HOMO is larger in the facial isomers whereas the iridium contribution to the LUMO is larger in the meridional complexes. The absorption spectra were simulated from the results of TD-DFT calculations; the absorption bands that corresponded to the metal-to-ligand charge transfer transitions and the intraligand π–π* transitions were well reproduced. At the vertical excitation $S_0 \rightarrow T_1$, the triplet state is highly delocalized among the ligands and has a mixed intraligand π–π* and MLCT character, which corresponds to electron transitions from HOMO to LUMO, LUMO+1, and LUMO+2. In the *fac*-isomers, the LUMO, LUMO+1, and LUMO+2 are localized on two or three ppy ligands, whereas in the *mer* isomers, these orbitals are localized on the single ppy ligand.

Quadratic response (QR) computations at the S_0 geometries were found to give satisfactory results compared to the experimental data; the phosphorescence radiative rate constants as well as the lifetimes are well reproduced. The computations suggest that the introduction of the fluorine atoms in the ppy ligand will lead to a larger HOMO–LUMO energy gap and blueshift in the emission energy. The spin–orbit coupling strength and the radiative rate constant are also diminished by the presence of the fluorine atoms, which could be attributed to the inverse heavy-atom effect. Moreover, the *fac*- and *mer*-[Ir($F_n$ppy)$_3$] complexes were found to exhibit similar phosphorescence wavelengths but different transition dipole moments, thereby resulting in notable differences in the radiative rate constants and lifetimes. Linear-response calculations also reveal that the SOC matrix element $\langle S_0 | \hat{H}_{SO} | T_1 \rangle$ is smaller in *fac*-[Ir($F_n$ppy)$_3$] than in *mer*-[Ir($F_n$ppy)$_3$], which indicates faster nonradiative quenching rate of the T_1 state in the latter complexes. It was also concluded that in the meridional isomer the SOC matrix element $\langle S_0 | \hat{H}_{SO} | T_1 \rangle$ together with the difference between the permanent dipole moments of the T_1 and S_0 states provide destructive contribution to the total $S_0 \rightarrow T_1$ transition moment, whereas in the facial complex such contribution is negligible.

With this work we show that quantum-chemical calculations at the time-dependent density-functional level of theory are useful for studies of iridium complexes, and can serve as a tool for building structure–property relationships and help synthesize even more efficient OLED dyes based on phosphorescence.

Theoretical Methods

In terms of the TD-DFT approach,[39,40,58] the excitation frequencies of the singlet–singlet transitions can be determined from the poles and the transition moments from the residues of the ground-state linear polarization propagator. The nonzero contribution to the $S_0 \rightarrow T_1$ transition moment originates from the first-order corrected wave functions

$$M_j^i = \sum_{n=0}^{\infty} \frac{\langle S_0|\hat{\mu}_j|S_n\rangle\langle S_n|\hat{H}_{SO}|T_1^i\rangle}{E(S_n)-E(T_1)} + \sum_{n=1}^{\infty} \frac{\langle S_0|\hat{H}_{SO}|T_n\rangle\langle T_n|\hat{\mu}_j|T_1^i\rangle}{E(T_n)-E(S_0)}, j \in \{x,y,z\} \quad (1)$$

which can be identified from the corresponding quadratic response (QR) function.[58] The spin sublevels of the triplet state in such a perturbation approach are considered to be degenerate. In Equation (1), the matrix elements of the electronic spin–orbit coupling operator $\hat{H}_{SO}$ include summation over intermediate triplet states with account of all three sublevels of each triplet. The representation of the triplet sublevels can be done in terms of the spin eigenfunctions with spin projection on the z axis, M_S, being a good quantum number. Any orthonormal set will do, since only the averaged lifetime [Equation (3)] is of interest in our case, which corresponds to the high-temperature limit. It is more useful to implement the Cartesian components of the triplet state, which are spin eigenfunctions with zero-spin projection on the corresponding axes,[59] since we consider the zero external magnetic-field case. Equation (1) can be evaluated by computing the single residue of the QR function; we refer to the literature for details.[60]

The spin–orbit coupling operator in Equation (1) is used here in the effective single-electron approximation suggested by Koseki et al.[13,61] In this approximation, the two-electron spin–orbit integrals are removed, which significantly reduces the computational time. It has been shown that the single-electron SOC operator combined with the use of effective core potentials (ECPs) can give phosphorescence lifetimes that are within 15% of the values obtained by a full relativistic four-component model.[62] All single-electron spin–orbit coupling integrals including two-center contributions from the metal atom and all ligands are taken into account in this approach.[13,61] The phosphorescence radiative rate constant k_r from one of the three sublevels (indexed by i) of the lowest triplet state can be expressed as[14]

$$k_r^i = k_r(S_0, T_1^i) = \frac{4\alpha_0^3}{3t_0} \Delta E_{S-T}{}^3 \sum_{j\in\{x,y,z\}} \left|M_j^i\right|^2 \quad (2)$$

where $t_0 = (4\pi\varepsilon_0)^2\hbar^3/m_e e^4$, a_0 is the fine-structure constant, ΔE_{S-T} is the transition energy, and M_j^i is the j axis projection ($j \in \{x, y, z\}$) of the electric dipole transition moment between the ground state and the i^{th} spin level of the triplet state.

Experimental studies of the [Ir($F_n$ppy)$_3$] complexes, calculated in the present work, have been performed in butyronitrile glass at 77 K and in dichloromethane at 298 K.[23] Though 77 K is usually considered to be low temperature, it is still much higher than that for the liquid helium, which is necessary to cool the sample, if one needs to resolve phosphorescence from individual spin sublevels.[20] On this basis, we have calculated the averaged phosphorescence lifetime, which corresponds to so-called high-temperature limit. The radiative lifetime τ of the triplet state in this limit, when spin-lattice relaxation equalizes the sublevel population before the phosphorescent emission occurs, is obtained by averaging over the three sublevels[11]

$$\frac{1}{\tau} = \frac{1}{3}\sum_{i=1}^{3}\frac{1}{\tau^i} = \frac{1}{3}\sum_{i=1}^{3}k_r^i \quad (3)$$

in which the nonradiative rate constant k_{nr} is not included. Therefore the lifetime τ thus computed can only be compared with the experimental lifetime measured in low-temperature glass or polymer matrix in which the quantum yield is close to unity.

To evaluate Equation (2), we first calculated the M_j^i transition moment from Equation (1) by the TD-DFT QR method.[58] The molecular structures of the iridium(III) complexes have been optimized for the singlet ground state and for the first triplet excited state. This has been done at the density functional theory level using the hybrid PBE0 exchange-correlation functional[63] with the LANL2DZ basis set[64] for iridium and the 6-31G* basis set[65] for the lighter atoms. For the calculations of frontier molecular orbitals and singlet–singlet excitation energies, we have used the same functional and basis set. The B3LYP functional[66] and the Stuttgart ECP basis sets (SDD)[67] for iridium have been used in the TD-DFT linear and quadratic response calculations for phosphorescence wavelength, radiative rate constant, and lifetime. Structure optimizations have been performed with the Gaussian 03 program,[68] whereas the phosphorescence calculations have been performed with the Dalton code.[39,40,58]

Acknowledgments

This work was supported by a grant from the Swedish Infrastructure Committee (SNIC) for the project *Multiphysics Modeling of Molecular Materials* (SNIC 022/09-25).

[1] M. A. Baldo, S. R. Forrest, *Phys. Rev. B* **2000**, *62*, 10958–10966.
[2] M. A. Baldo, D. F. O'Brien, Y. You, A. Shoustikov, S. Sibley, M. E. Thompson, S. R. Forrest, *Nature* **1998**, *395*, 151–154.
[3] M. A. Baldo, S. Lamansky, P. E. Burrows, M. E. Thompson, S. R. Forrest, *Appl. Phys. Lett.* **1999**, *75*, 4–6.
[4] J. S. Wilson, A. S. Dhoot, A. J. A. B. Seeley, M. S. Khan, A. Köhler, R. H. Friend, *Nature* **2001**, *413*, 828–831.
[5] M. Wohlgenannt, K. Tandon, S. Mazumdar, S. Ramasesha, Z. V. Vardeny, *Nature* **2001**, *409*, 494–497.
[6] D. Veldman, S. M. A. Chopin, S. C. J. Meskers, M. M. Groeneveld, R. M. Williams, R. A. J. Janssen, *J. Phys. Chem. A* **2008**, *112*, 5846–5857.
[7] Z. E. X. Dance, Q. Mi, D. W. McCamant, M. J. Ahrens, M. A. Ratner, M. R. Wasielewski, *J. Phys. Chem. B* **2006**, *110*, 25163–25173.
[8] B. Minaev, E. Jansson, H. Ågren, S. Schrader, *J. Chem. Phys.* **2006**, *125*, 234704.
[9] S. Knuts, B. F. Minaev, H. Ågren, O. Vahtras, *Theor. Chim. Acta* **1994**, *87*, 343–371.
[10] B. F. Minaev, D. Jonsson, P. Norman, H. Ågren, *Chem. Phys.* **1995**, *194*, 19–31.
[11] H. Ågren, O. Vahtras, B. Minaev, *Adv. Quantum Chem.* **1996**, *27*, 71–162.
[12] Y. Cao, I. D. Parker, G. Yu, C. Zhang, A. J. Heeger, *Nature* **1999**, *397*, 414–417.
[13] S. Koseki, D. G. Fedorov, M. W. Schmidt, M. S. Gordon, *J. Phys. Chem. A* **2001**, *105*, 8262–8268.
[14] E. Jansson, B. Minaev, S. Schrader, H. Ågren, *Chem. Phys.* **2007**, *333*, 157–167.
[15] M. A. Baldo, C. Adachi, S. R. Forrest, *Phys. Rev. B* **2000**, *62*, 10967–10977.
[16] M. A. Baldo, D. F. O'Brien, M. E. Thompson, S. R. Forrest, *Phys. Rev. B* **1999**, *60*, 14422–14428.
[17] P. J. Hay, *J. Phys. Chem. A* **2002**, *106*, 1634–1641.
[18] K. Nozaki, *J. Chin. Chem. Soc.* **2006**, *53*, 101–112.
[19] G. J. Hedley, A. Ruseckas, I. D. W. Samuel, *J. Phys. Chem. A* **2009**, *113*, 2–4.

[20] W. J. Finkenzeller, H. Yersin, *Chem. Phys. Lett.* **2003**, *377*, 299–305.
[21] T. Abe, A. Miyazawa, H. Konno, Y. Kawanishi, *Chem. Phys. Lett.* **2010**, *491*, 199–202.
[22] G. J. Hedley, A. Ruseckas, I. D. W. Samuel, *J. Phys. Chem. A* **2010**, *114*, 8961–8968.
[23] R. Ragni, E. A. Plummer, K. Brunner, J. W. Hofstraat, F. Babudri, G. M. Farinola, F. Naso, L. De Cola, *J. Mater. Chem.* **2006**, *16*, 1161–1170.
[24] B. Minaev, H. Ågren, F. De Angelis, *Chem. Phys.* **2009**, *358*, 245–257.
[25] A. P. Monkman, H. D. Burrows, I. Hamblett, S. Navaratnam, *Chem. Phys. Lett.* **2001**, *340*, 467–472.
[26] D. Xu, D. Xie, H. Guo, *J. Chem. Phys.* **2002**, *116*, 10626–10635.
[27] Y.-Y. Noh, C.-L. Lee, J.-J. Kim, K. Yase, *J. Chem. Phys.* **2003**, *118*, 2853–2864.
[28] M. L. Xu, R. Zhou, G. Y. Wang, Q. Xiao, W. S. Du, G. B. Che, *Inorg. Chim. Acta* **2008**, *361*, 2407–2412.
[29] *Highly Efficient OLEDs with Phosphorescent Materials* (Ed.: H. Yersin), Wiley-VCH, Weinheim, Germany, **2007**.
[30] J. Slinker, D. Bernards, P. L. Houston, H. D. Abruña, S. Bernhard, G. G. Malliaras, *Chem. Commun.* **2003**, 2392–2399.
[31] N. G. Park, G. C. Choi, Y. H. Lee, Y. S. Kim, *Curr. Appl. Phys.* **2006**, *6*, 620–626.
[32] F. De Angelis, S. Fantacci, N. Evans, C. Klein, S. M. Zakeeruddin, J.-E. Moser, K. Kalyanasundaram, H. J. Bolink, M. Graetzel, Md. K. Nazeeruddin, *Inorg. Chem.* **2007**, *46*, 5989–6001.
[33] H. J. Bolink, E. Coronado, S. G. Santamaria, M. Sessolo, N. Evans, C. Klein, E. Baranoff, K. Kalyanasundaram, M. Graetzel, Md. K. Nazeeruddin, *Chem. Commun.* **2007**, 3276–3278.
[34] I. Avilov, P. Minoofar, J. Cornil, L. De Cola, *J. Am. Chem. Soc.* **2007**, *129*, 8247–8258.
[35] E. Baranoff, S. Suàrez, P. Bugnon, C. Barolo, R. Buscaino, R. Scopelliti, L. Zuppiroli, M. Graetzel, Md. K. Nazeeruddin, *Inorg. Chem.* **2008**, *47*, 6575–6577.
[36] D. Di Censo, S. Fantacci, F. De Angelis, C. Klein, N. Evans, K. Kalyanasundaram, H. J. Bolink, M. Grätzel, Md. K. Nazeeruddin, *Inorg. Chem.* **2008**, *47*, 980–989.
[37] S. Lamansky, P. Djurovich, D. Murphy, F. Abdel-Razzaq, R. Kwong, I. Tsyba, M. Bortz, B. Mui, R. Bau, M. E. Thompson, *Inorg. Chem.* **2001**, *40*, 1704–1711.
[38] Y. You, S. Y. Park, *J. Am. Chem. Soc.* **2005**, *127*, 12438–12439.
[39] *DALTON*, rel. 2.0, **2005**, http://daltonprogram.org.
[40] O. Vahtras, H. Ågren, P. Jørgensen, H. J. A. Jensen, T. Helgaker, J. Olsen, *J. Chem. Phys.* **1992**, *97*, 9178–9187.
[41] J. Breu, P. Stössel, S. Schrader, A. Starukhin, W. J. Finkenzeller, H. Yersin, *Chem. Mater.* **2005**, *17*, 1745–1752.
[42] R. J. F. Berger, H.-G. Stammler, B. Neumann, N. W. Mitzel, *Eur. J. Inorg. Chem.* **2010**, 1613–1617.
[43] F. O. Garces, K. Dedeian, N. L. Keder, R. J. Watts, *Acta Crystallogr., Sect. C* **1993**, *49*, 1117–1120.
[44] D. Nie, Z. Liu, Z. Bian, C. Huang, *THEOCHEM* **2008**, *861*, 97–102.
[45] X. Li, Q. Zhang, Y. Tu, H. Ågren, H. Tian, *Phys. Chem. Chem. Phys.* **2010**, *12*, 13730–13736.
[46] A.-R. Allouche, *J. Comput. Chem.* **2011**, *32*, 174–182.
[47] T. Liu, B.-H. Xia, X. Zhou, H.-X. Zhang, Q.-J. Pan, J.-S. Gao, *Organometallics* **2007**, *26*, 143–149.
[48] T. Liu, B.-H. Xia, Q.-C. Zheng, X. Zhou, Q.-J. Pan, H.-X. Zhang, *J. Comput. Chem.* **2010**, *31*, 628–638.
[49] B. Minaev, V. Minaeva, H. Ågren, *J. Phys. Chem. A* **2009**, *113*, 726–735.
[50] V. Barone, M. Cossi, *J. Phys. Chem. A* **1998**, *102*, 1995–2001.
[51] M. Cossi, G. Scalmani, N. Rega, V. Barone, *J. Comput. Chem.* **2003**, *24*, 669–681.
[52] T. Hofbeck, H. Yersin, *Inorg. Chem.* **2010**, *49*, 9290–9299.
[53] H. Saigusa, T. Azumi, *J. Chem. Phys.* **1979**, *71*, 1408–1413.
[54] H. Saigusa, T. Azumi, M. Sumitani, K. Yoshihara, *J. Chem. Phys.* **1980**, *72*, 1713–1715.
[55] B. F. Minaev, S. Knuts, H. Ågren, *Chem. Phys.* **1994**, *181*, 15–28.
[56] S. Yamauchi, Y. Matsukawa, Y. Ohba, M. Iwaizumi, *Inorg. Chem.* **1996**, *35*, 2910–2914.
[57] Z. Havlas, J. Michl, *J. Am. Chem. Soc.* **2002**, *124*, 5606–5607.
[58] B. Minaev, H. Ågren, *Chem. Phys.* **2005**, *315*, 215–239.
[59] B. Minaev, I. Tunnell, P. Salek, O. Loboda, O. Vahtras, H. Ågren, *Mol. Phys.* **2004**, *102*, 1391–1406.
[60] I. Tunell, Z. Rinkevicius, O. Vahtras, P. Sałek, T. Helgaker, H. Ågren, *J. Chem. Phys.* **2003**, *119*, 11024–11034.
[61] S. Koseki, M. W. Schmidt, M. S. Gordon, *J. Phys. Chem. A* **1998**, *102*, 10430–10435.
[62] E. Jansson, P. Norman, B. Minaev, H. Ågren, *J. Chem. Phys.* **2006**, *124*, 114106.
[63] J. P. Perdew, K. Burke, M. Ernzerhof, *Phys. Rev. Lett.* **1996**, *77*, 3865–3868.
[64] P. J. Hay, W. R. Wadt, *J. Chem. Phys.* **1985**, *82*, 299–310.
[65] W. J. Hehre, R. Ditchfield, J. A. Pople, *J. Chem. Phys.* **1972**, *56*, 2257–2261.
[66] A. D. Becke, *J. Chem. Phys.* **1993**, *98*, 5648–5652.
[67] D. Andrae, U. Häußermann, M. Dolg, H. Stoll, H. Preuß, *Theor. Chim. Acta* **1990**, *77*, 123–141.
[68] M. J. Frisch, G. W. Trucks, H. B. Schlegel, G. E. Scuseria, M. A. Robb, J. R. Cheeseman, J. A. Montgomery Jr., T. Vreven, K. N. Kudin, J. C. Burant, J. M. Millam, S. S. Iyengar, J. Tomasi, V. Barone, B. Mennucci, M. Cossi, G. Scalmani, N. Rega, G. A. Petersson, H. Nakatsuji, M. Hada, M. Ehara, K. Toyota, R. Fukuda, J. Hasegawa, M. Ishida, T. Nakajima, Y. Honda, O. Kitao, H. Nakai, M. Klene, X. Li, J. E. Knox, H. P. Hratchian, J. B. Cross, V. Bakken, C. Adamo, J. Jaramillo, R. Gomperts, R. E. Stratmann, O. Yazyev, A. J. Austin, R. Cammi, C. Pomelli, J. W. Ochterski, P. Y. Ayala, K. Morokuma, G. A. Voth, P. Salvador, J. J. Dannenberg, V. G. Zakrzewski, S. Dapprich, A. D. Daniels, M. C. Strain, O. Farkas, D. K. Malick, A. D. Rabuck, K. Raghavachari, J. B. Foresman, J. V. Ortiz, Q. Cui, A. G. Baboul, S. Clifford, J. Cioslowski, B. B. Stefanov, G. Liu, A. Liashenko, P. Piskorz, I. Komaromi, R. L. Martin, D. J. Fox, T. Keith, M. A. Al-Laham, C. Y. Peng, A. Nanayakkara, M. Challacombe, P. M. W. Gill, B. Johnson, W. Chen, M. W. Wong, C. Gonzalez, J. A. Pople, *Gaussian 03*, rev. D.01, Gaussian, Inc., Wallingford CT, **2004**.

Received: January 24, 2011
Published Online: April 18, 2011

